#### **ORIGINAL ARTICLE**



# Original and liposome-modified indocyanine green—assisted fluorescence study with animal models

Zheng Li<sup>1</sup> · Zhongqiang Li<sup>1</sup> · Yuting Yang<sup>2</sup> · Shaomian Yao<sup>3</sup> · Chaozheng Liu<sup>4</sup> · Jian Xu<sup>1</sup>

Received: 27 March 2023 / Accepted: 5 June 2023 © The Author(s), under exclusive licence to Springer-Verlag London Ltd., part of Springer Nature 2023

#### **Abstract**

Medical diagnosis heavily relies on the use of bio-imaging techniques. One such technique is the use of ICG-based biological sensors for fluorescence imaging. In this study, we aimed to improve the fluorescence signals of ICG-based biological sensors by incorporating liposome-modified ICG. The results from dynamic light scattering and transmission electron microscopy showed that MLM-ICG was successfully fabricated with a liposome diameter of 100–300 nm. Fluorescence spectroscopy showed that MLM-ICG had the best properties among the three samples (Blank ICG, LM-ICG, and MLM-ICG), as samples immersed in MLM-ICG solution achieved the highest fluorescence intensity. The NIR camera imaging also showed a similar result. For the rat model, the best period for fluorescence tests was between 10 min and 4 h, where most organs reached their maximum fluorescence intensity except for the liver, which continued to rise. After 24 h, ICG was excreted from the rat's body. The study also analyzed the spectra properties of different rat organs, including peak intensity, peak wavelength, and FWHM. In conclusion, the use of liposome-modified ICG provides a safe and optimized optical agent, which is more stable and efficient than non-modified ICG. Incorporating liposome-modified ICG in fluorescence spectroscopy could be an effective way to develop novel biosensors for disease diagnosis.

**Keywords** Indocyanine Green · Liposome-modified ICG · Near-infrared imaging · Fluorescence spectrum

#### Introduction

Biomedical data including images and spectra play a significant role in diagnosing diseases [1–4]. Among various biomedical imaging techniques, fluorescence imaging stands out as one of the most popular methods. This technique normally uses a dye that can generate fluorescence to achieve the image contrast between the target and control. When the excitation light shines on the dyed specimen, fluorescent

signals will be emitted and can be captured by optical sensors, such as a camera and spectrometer. Moreover, one-dimensional spectra, such as fluorescence and Raman spectra, have also demonstrated their applicability for numerous biomedical applications [5–8].

Indocyanine green (ICG) is a widely used fluorescent agent due to its excellent fluorescence property and rapid absorption and excretion mechanisms, making it applicable for both in vivo and ex vivo medical fields. ICG-assisted diagnosis has become a standard practice in the in vivo imaging studies, such as neurovascular surgery [9]. In ex vivo imaging, most research is pilot studies exploring the possibility of using ICG-assisted disease diagnosis. ICG molecules bond to plasma proteins and lipoproteins, such as human serum albumin, show enhanced fluorescence ability [10]. ICG molecules circulate through the body and are removed by the liver to the bile juice [11, 12]. However, ICG may fail to identify the differences between normal and malignancy in some cases because of its unsteady and easily quenched properties [13, 14]. Moreover, the ICG molecules have difficulty penetrating the cell due to the cell membrane channel selection [15, 16].

☑ Jian Xu jianxu1@lsu.edu

Published online: 17 June 2023

- Division of Electrical and Computer Engineering, College of Engineering, Louisiana State University, LA70803, Baton Rouge, USA
- Khoury College of Computer Sciences, Northeastern University, MA02115, Boston, USA
- Department of Comparative Biomedical Science, School of Veterinary Medicine, Louisiana State University, LA70803, Baton Rouge, USA
- School of Renewable Natural Resources, Louisiana State University AgCenter, Baton Rouge, LA 70803, USA



Cell membranes are composed of lipid bilayers with various gates that selectively allow specific ions or molecules to enter or exit the cell. However, there is no specific channel for ICG molecules. Liposomes, which have a structure similar to lipid bilayers, can aid in the penetration of cell membranes when combined with other molecules. Specific ligands can be added to the liposome to increase uptake and selectivity for particular targets [17]. Additionally, liposomes have been used as drug carriers for the treatment of viral or infectious diseases [18]. Moreover, liposome-encapsulated ICG was fabricated for sentinel lymph node imaging with the traditional hydration and extrusion method [19]. 5-aminolevulinic acid liposomal formulated ICG has been investigated for the analysis of brain tumor margins using NIR light [20].

NIR light, which includes NIR-I (700-950 nm) and NIR-II (950-2000 nm), has enhanced penetrative ability, allowing photons to penetrate deep into tissues. The excitation and emission wavelength peaks of ICG are around 789 nm and 814 nm, respectively. ICG-assisted NIR imaging systems have tremendous potential for novel, cost-effective, and non-invasive disease diagnosis [21, 22]. Additionally, NIR imaging decreases light scattering on the tissue surface, which reduces auto-fluorescence [23, 24]. The penetration depth of NIR light is approximately 10 mm, providing significant advantages in detecting soft tissues [25, 26]. Apart from imaging, the fluorescence spectrum can also demonstrate various sample properties through the peak intensity and shift. The fluorescence spectrum peak represents the intensity of the optical agents and is a rapid and efficient way to identify target and control. Moreover, the full-width half maximum (FWHM) is also an important feature of the spectrum.

This study investigated the optimal imaging window (duration from injection to imaging) by intravenously injecting the ICG solution into a rat model and collecting fluorescence spectra of different organs. Furthermore, liposome-modified ICG (LM-ICG) and mannose liposome-modified ICG (MLM-ICG) were developed and applied to pork tissues. The results showed that the modified ICG served as an

excellent imaging agent in animal models, demonstrating potential applications for human disease diagnoses.

#### **Materials and methods**

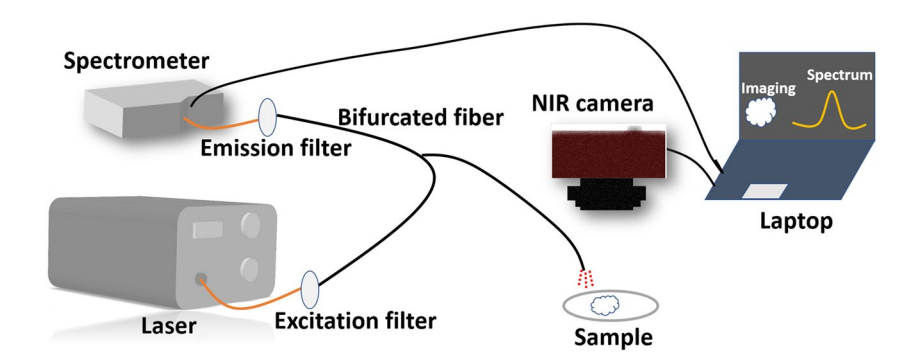
#### **Materials**

The ICG, L-a-phosphatidylcholine (Egg-PC), and L-a-phosphatidylethanolamine (Egg-PE) were purchased from Sigma-Aldrich (St. Louis, MO), while cholesterol, D-(+)-mannose, chloroform, and methanol were purchased from Alfa Aesar (Haverhill, MA). The pork fat and pork muscle were obtained from Albertson's market (Baton Rouge, LA). The mini extruder used in the study was from Avanti Polar Lipids (Alabaster, AL). The dynamic light scattering analysis was conducted using MicroTrac S3500 and ZetaTrac instruments at the Composite Engineering Laboratory, School of Renewable Natural Resources, LSU. The transmission electron microscopy was performed using JEM-1400 TEM (120v, JEOL, Peabody, MA).

Figure 1 illustrates the imaging system used in this study, which is similar to the setup used in previous studies [21, 22, 27]. The system consists of a bifurcated optical fiber that is connected to a 785-nm laser source and a spectrometer. The laser light is directed at the samples through the output of the fiber. The spectrometer and NIR-I camera are also connected to the fiber and are equipped with an 800-nm long-pass filter. The camera is positioned vertically above the sample to capture fluorescent signals, and both the spectrometer and camera are connected to a computer for data collection.

Pork muscle and fat samples were cut into  $1.0 \times 1.0 \times 0.3$  cm<sup>3</sup> pieces and immersed in ICG solution for 10 min before imaging. The camera was placed approximately 25 cm away from the samples, and the fluorescent signals were collected and averaged over five measurements at each spot. The spectra were then smoothed using a seven-span filter in MAT-LAB R2019a (MathWorks Inc.). The fluorescent images of the pork and fat samples were extracted and cropped from the NIR videos without any further processing.

**Fig. 1** Schematic diagram of NIR imaging system





Lasers in Medical Science (2023) 38:140 Page 3 of 8 140

### Syntheses of modified ICG with liposomes

The liposome-modified ICG (LM-ICG) was synthesized using the following procedure: Egg-PC, cholesterol, and Egg-PE (molar ratio = 7:2:1) were dissolved in a mixture of chloroform and methanol (volume ratio = 7:3). The resulting solution was evaporated at room temperature overnight, forming a thin transparent film. Next, 10 mL of ICG solution (20 µmol) was added to the film and allowed to hydrate for 10 min. The solution was then frozen using liquid nitrogen and thawed six times before being extruded ten times through a mini extruder loaded with a 100-nm polycarbonate film. The resulting liposome mixture was purified using column chromatography with a PD Midi-Trap G-25 column. Mannose liposome-modified ICG (MLM-ICG) was prepared using the same procedure as LM-ICG, with the exception of the hydrated solution and chromatographic eluent, which were both supplemented with 5% (w/v) mannose.

#### **Animals**

A total of 18 animals were included in this study, consisting of four nude mice and 14 self-breed Sprague Dawley rats. Three of the nude mice were intravenously injected with an ICG solution with a concentration of 0.22 mg/kg, while the fourth mouse served as the control and did not receive an ICG injection. The rat model included 13 postnatal rats that were injected with 5 mg/kg ICG solution via the tail vein at different imaging windows (10 min, 4 h, and 24 h), with one rat serving as the control. All animals were sacrificed for the study, and their specimens were resected and imaged ex vivo.

All animal experiments were conducted in accordance with ethical guidelines and were authorized by the Institutional Animal Care and Use Committee (IACUC) of Louisiana State University (Protocol# 16-117, 17-033, 20-046). The care and use of animals followed strict ethical guidelines, ensuring their welfare throughout the study.

#### **Image contrast**

As previously defined, image contrast aims to quantitatively illustrate the optical difference between the target and background regions [28–31]. To calculate image contrast, a line is drawn on both the target and background regions, and the pixel values of the line are extracted. The following equation is then used to calculate image contrast:

$$\text{Image contrast} = avg \left( \sum_{i=0}^{n} \frac{\left( g\_val_t - g\_val_b \right)}{0.5 * \left( avg \left( \sum_{i=0}^{n} g\_val_t \right) + avg \left( \sum_{i=0}^{n} g\_val_b \right) \right)} \right)$$

n is the pixel number of the line,  $g\_val_t$  is the target pixel value, and  $g\_val_b$  is the background pixel value.

#### Results

# Morphology and fluorescent property of the modified ICG

The size distribution of MLM-ICG liposomes was analyzed using dynamic light scattering (DLS), and the results are presented in Fig. 2a. The DLS machine was thoroughly cleaned before the modified ICG was slowly added to the container. After approximately 5 min, the monitor curve and analysis chart were generated. The percentage distributions of the liposomes were determined, with 34.9% of the liposomes measuring 102 nm, 39.88% measuring 122 nm, and 20.39% measuring 145 nm. The majority of liposome diameters fell between 100 and 200 nm, which was consistent with the pore size of the polycarbonate filter (100 nm). The size distributions of LM-ICG liposomes are included in the supplement file (Fig. S1) and indicate larger sizes (over 200 nm) than those of MLM-ICG liposomes.

Figure 2b and c depicted the structure and morphology of the modified ICG. The modified ICG was prepared following the traditional vesicle preparation process before TEM imaging. Specifically, a drop of the modified ICG was placed on a copper grid, added with uranyl acetate solution (2%), and the staining solution was removed [32]. The TEM images of both LM-ICG (supplement file, Fig. S2) and MLM-ICG (Fig. 2b) revealed the presence of liposomes, with the latter showing more liposomes. The size of the MLM-ICG liposomes ranged from 100 to 200 nm (Fig. 2c), with an insert image showing a typical liposome diameter of 89.4 nm. In contrast, the diameter of LM-ICG was several hundred nanometers.

Figure 3a showed the fluorescence intensity of the modified ICG solutions, including blank ICG, LM-ICG, and MLM-ICG. The liposome-modified ICG solutions maintained their excellent fluorescent ability, with MLM-ICG showing a higher intensity compared to LM-ICG. Although the concentration of the modified ICG could not be accurately detected after extrusion and column chromatography, the original ICG solution was diluted 10 times to obtain a similar fluorescence intensity as the modified ICG solutions (purple line in Fig. 3a). A diluted ICG solution with 4% (w/v) bull serum albumin (BSA) was also prepared for comparison because BSA could improve the fluorescence property of ICG solutions for animal experiments. Figure 3b illustrated the peak wavelength of the diluted ICG solution changed from 807 to 815 nm after adding BSA (error bar from 5 spectra). The full width at half maximum (FWHM) of the diluted ICG solution and ICG with BSA solution were 37.71 nm and 45.98 nm, respectively.

Pork muscle and fat samples were treated with blank ICG solution, LM-ICG solution, and MLM-ICG solution



140 Page 4 of 8 Lasers in Medical Science (2023) 38:140

Fig. 2 Morphology of MLM-ICG: diameter distributions through DLS analysis (a); TEM images: 1 µm (b); and 200 nm (c)

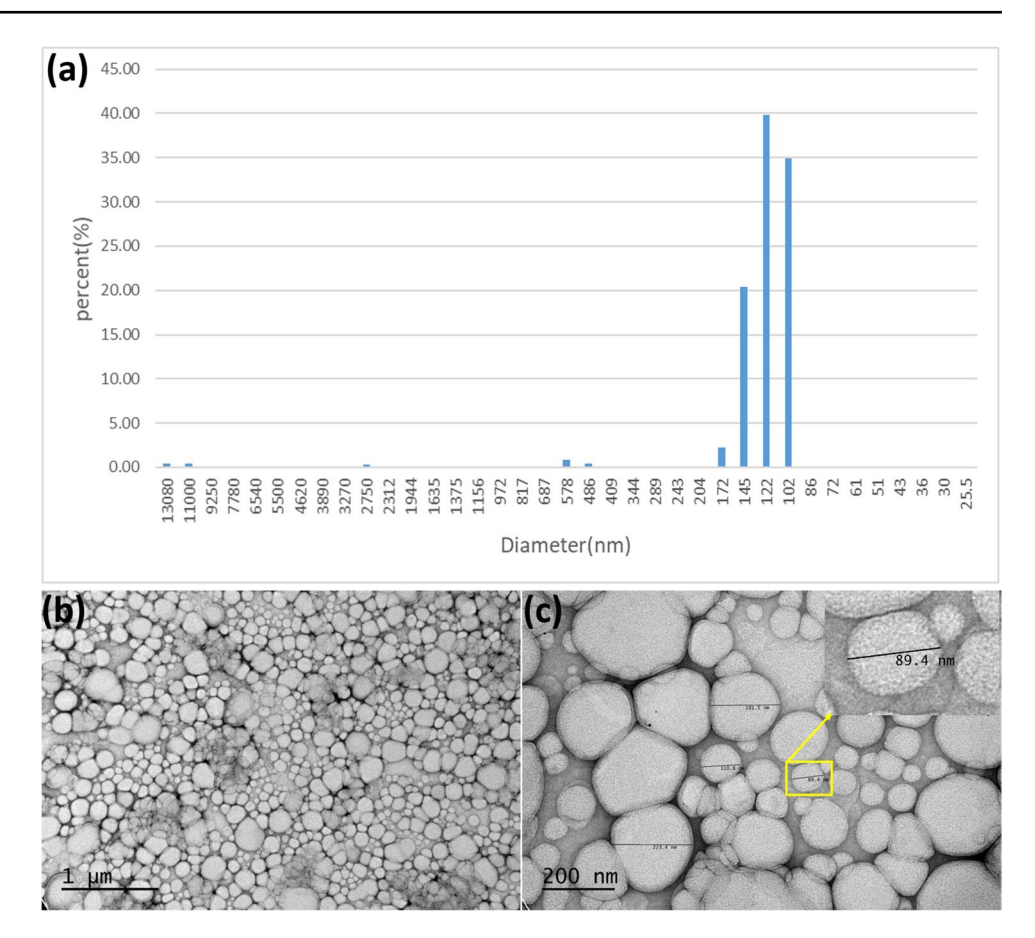
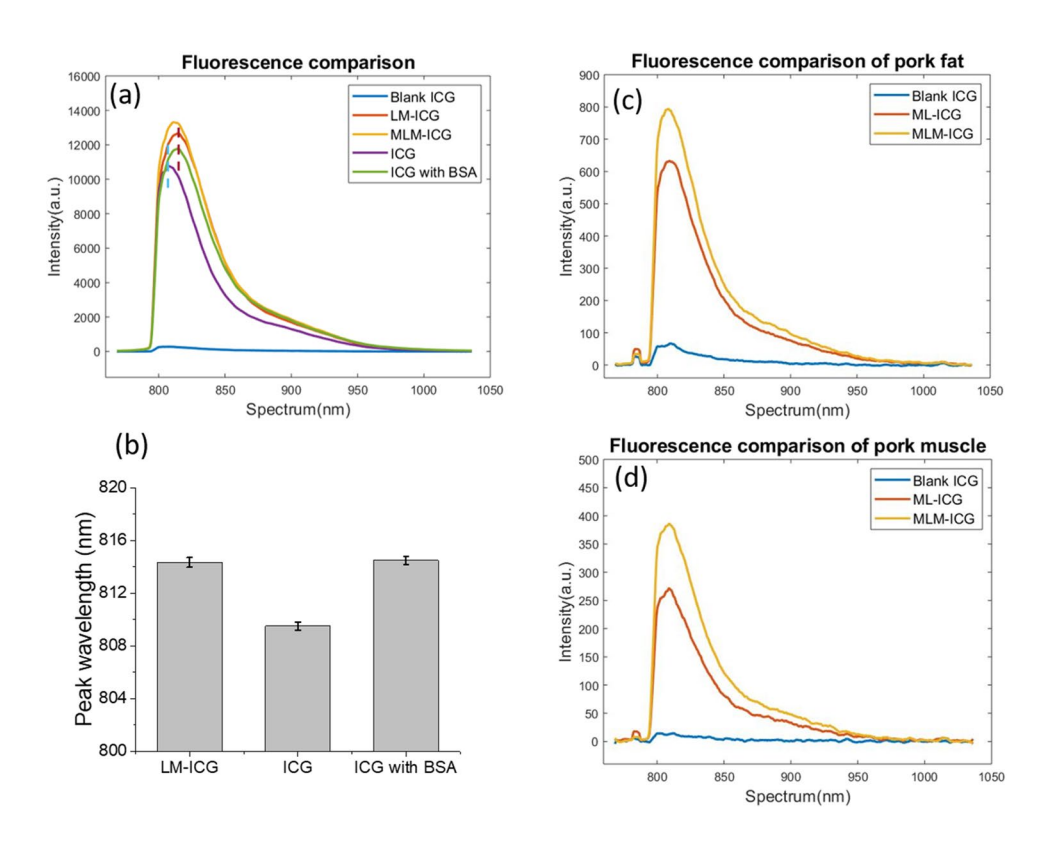


Fig. 3 The spectrum of modified ICG: fluorescence comparison of blank ICG, LM-ICG, MLM-ICG, ICG solution, and ICG solution with BSA (a) and peak wavelength (b); fluorescence comparison of pork muscle (c) and fat (d) immersed with blank ICG, LM-ICG, and MLM-ICG solution





Lasers in Medical Science (2023) 38:140 Page 5 of 8 140

for 10 min before imaging. The fluorescence intensity of the muscle and fat samples treated with blank ICG solution was the weakest, while MLM-ICG performed better than LM-ICG (Fig. 3c, d). One possible reason for MLM-ICG's better fluorescence ability is that the smaller size of the liposomes in the mannose-modified ICG solution could penetrate the tissues more easily. Moreover, fat tissue has a higher lipid content compared to muscle tissue, indicating that ICG and liposome-modified ICG are more likely to be absorbed by fat tissue.

To further investigate the properties of the modified ICG solutions, we applied NIR-I imaging to pork fat and muscle after immersion in the ICG solutions. As expected, tissues treated with the blank ICG solution showed almost no fluorescence signal (Fig. 4a, b). However, both LM-ICG and MLM-ICG solutions exhibited excellent fluorescence, with MLM-ICG displaying brighter fluorescence than LM-ICG. Furthermore, fat tissue exhibited stronger fluorescence signals than muscle tissue, consistent with the spectra shown in Fig. 3. The image contrast analysis further confirmed these results (Fig. 4g).

# Spectrum analysis of ICG with the animal model

We investigated the fluorescence properties of ICG-assisted imaging under various experimental conditions, including peak intensity, peak wavelength, and FWHM. As shown in Fig. 5a, we found that the fluorescent intensity of fat was greater than that of muscle in the mice model, which was consistent with the results obtained from the pork muscle and fat experiments. In the rat model, we identified the optimal imaging windows for observing the ICG-assisted optical properties of various organs, including the lung, heart, liver, stomach, and kidney, over 10 min, 4 h, and 24 h (Fig. 5b–d). Our results revealed that the spectrum of 10 min exhibited a strong intensity, indicating that the ICG solution could

be rapidly distributed throughout the organs. However, the fluorescence of each organ began to decrease, except for the liver, at 4 h (Fig. 5c). Notably, the liver showed extremely high fluorescent intensity due to the transmission of ICG from other organs and subsequent excretion from the liver. After 24 h, the fluorescence greatly decreased, indicating that most of the ICG was excreted from the body (Fig. 5d).

Figure S3 presented the fluorescence spectrum properties of the organs at 10 min, 4 h, and 24 h. The peak wavelength of 10 min was consistently around 822 nm (Fig. S3d), whereas it decreased at 4 and 24 h (Fig. S3e–f), particularly for the lung and stomach. Additionally, Fig. S3g–i illustrates the FWHM of each organ at different imaging windows. The FWHM of the lung, heart, and kidney were more consistent than that of the liver and stomach in terms of intensity.

#### **Discussions**

In our previous work, we studied ICG-assisted dental imaging using a rat model and a human-extracted teeth model, and achieved improvements such as identifying cracks and caries that were difficult to detect using X-ray imaging [33]. However, one limitation we noted in our previous report [28] was that ICG was unable to illustrate un-erupted molars due to its unstable and easily agglomerated nature, which limited its application in deeper biomedical imaging. Liposomemodified ICG can address this limitation by separating ICG molecules. Moreover, the use of biocompatible liposomes and FDA-approved ICG generate a risk-free combination for biomedical imaging.

The liposome sizes of LM-ICG and MLM-ICG particles were measured using the DLS test and TEM images. While DLS provides an estimate of size, TEM allows for more accurate size distribution measurements

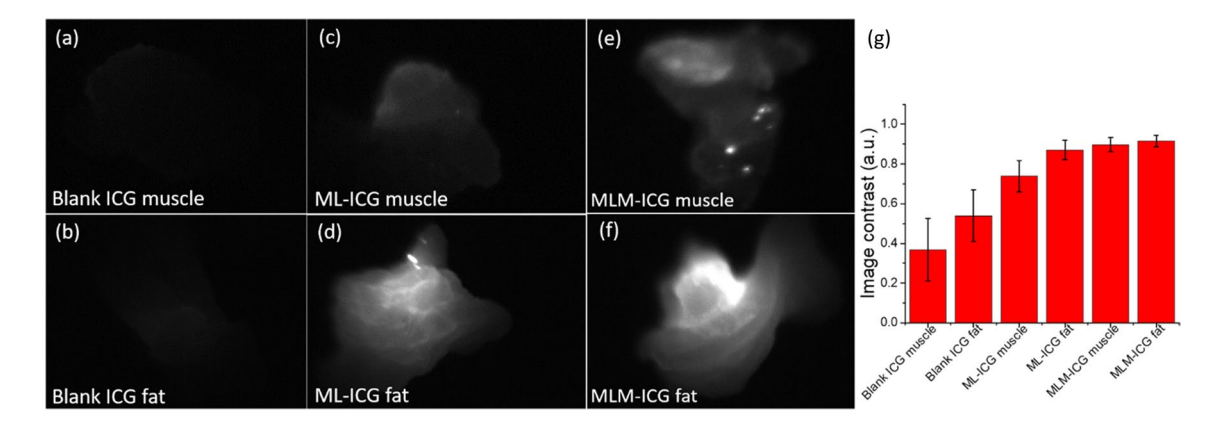


Fig. 4 ICG-assisted NIR I images of pork muscle and fat immersed with blank ICG (a, b), LM-ICG (c, d), and MLM-ICG solution (e, f) with image contrast (g)



140 Page 6 of 8 Lasers in Medical Science (2023) 38:140

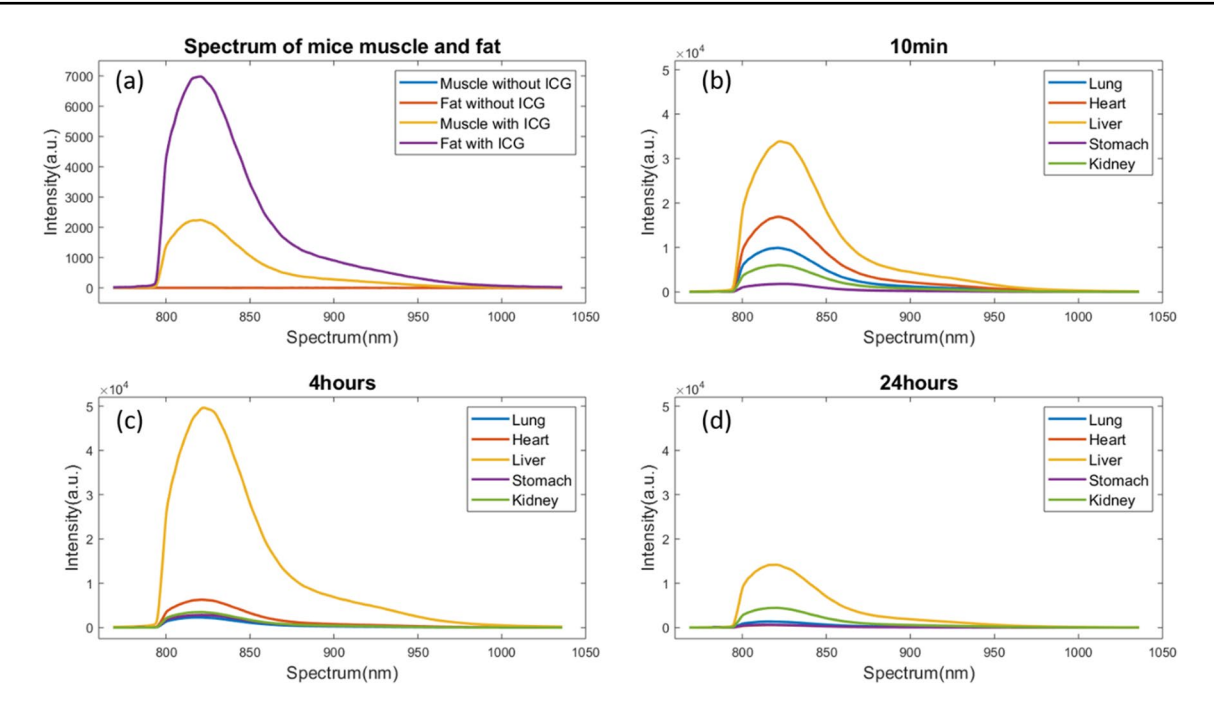


Fig. 5 ICG assisted fluorescence spectrum of mice muscle and fat without ICG vs. with ICG (a); rat organs (lung, heart, liver, stomach, and kidney) of different imaging windows (b-d)

as the particle diameter can be directly measured from the images. The TEM images showed that MLM-ICG had a more distinguishable and smaller size compared to LM-ICG, indicating that adding mannose during liposome fabrication improves the liposomes' morphology. Although some liposomes had diameters larger than the nano-scale due to the 100 nm polycarbonate filter used, the modified ICG still demonstrated excellent fluorescence ability. The low concentration of ICG solution (20 µmol) did not hinder the successful combination of massive ICG molecules with liposomes. In contrast, unmodified ICG molecules tended to aggregate and form large particles, which deposited on the filter support and polycarbonate membrane or were wasted on the column of chromatography. The modified ICG molecules were small and separated, resulting in strong fluorescent intensity. Compared to the original ICG solution, the peak wavelengths of modified ICG and ICG with BSA increased by ~24 nm and 6 nm, respectively, and FWHMs increased by 5.92 nm and 6.79 nm. The optical properties of ICG were altered by combining it with BSA or modifying it with liposomes, as evidenced by changes in spectral features such as peak shifts and FWHMs.

To study the fluorescent ability of modified ICG solutions in tissue, both pork fat and muscle were immersed in the solutions and imaged using NIR imaging and spectra. The LM-ICG and MLM-ICG solutions exhibited excellent fluorescent ability in the tissues compared to the blank ICG solution. However, due to the complex fabrication procedures involved in preparing the liposome-modified

ICG solution, it was difficult to directly compare it to the normal ICG solution. Additionally, the results showed that ICG was more easily absorbed by fat than muscle in both pork tissue and mouse models. This could be attributed to the fact that fat contains more lipids than muscle.

In addition to its potential use in dental imaging, indocyanine green (ICG) has shown promise in the diagnosis of other diseases, such as cancer. However, achieving the optimal fluorescent effect in human clinical studies requires careful consideration of factors such as the imaging window and injection dosage. Animal studies can provide valuable insights into the optimal imaging conditions for different organs in humans. To this end, we used a rat model to monitor the ICG imaging windows and spectrum, and identified the period between 10 min and 4 h post-injection as the time frame with strong fluorescent intensities in rat organs. We also observed that most of the ICG was excreted after 24 h. These findings have important implications for future human studies involving ICG imaging.

#### **Conclusions**

This study investigated the potential of liposome-modified indocyanine green (LM-ICG) as a bio-imaging dye. Both LM-ICG and mannose-modified ICG (MLM-ICG) showed excellent fluorescent ability in pork tissues compared to the blank ICG solution. The liposome-modified ICG solution demonstrated similar effects to the ICG solution mixed



Lasers in Medical Science (2023) 38:140 Page 7 of 8 140

with BSA. The liposomes helped LM-ICG combine with or penetrate the cell membrane, potentially making it an optimized bio-imaging dye due to its enhanced fluorescent ability and improved signals. Additionally, the imaging windows and injection dosage of ICG were explored in a rat model. Results indicated that the best imaging windows for rat organs were between 10 min and 4 h, and most of the ICG was excreted after 24 h. The peak intensity, peak wavelength, and FWHM of the fluorescence spectrum were also identified as important features for spectra analysis. Overall, this work has demonstrated the potential of LM-ICG for various biomedical imaging applications, including dental disorders and cancer diagnosis.

**Supplementary Information** The online version contains supplementary material available at https://doi.org/10.1007/s10103-023-03802-5.

**Author contributions** ZL and JX did the conceptualization and methodology. CL helped with the software. ZL and ZqL wrote the original draft. YY, SY, and JX reviewed and edited the manuscript. All authors have read and agreed to the published version of the manuscript.

Funding This research was supported by the NIH (1U01AA029348-01), NSF CAREER award (2046929), Louisiana State University (LSU) Faculty Research Grants (009875), LSU Collaborative Cancer Research Initiative (010163), LSU Provost's Fund for Innovation in Research-Faculty Research Grants-Big Idea Research Planning Grants Phase 2 (PG010215), LSU Leveraging Innovation for Technology Transfer (LIFT2) Grant (LSU-2020-LIFT-008), and Louisiana Board of Regents Grant (LEQSF (2018-21)-RD-A-09).

#### **Declarations**

Competing interests The authors declare no competing interests.

# References

- Atta D, Okasha A (2015) Single molecule laser spectroscopy. Spectrochim Acta A Mol. Biomol 135:1173–1179. https://doi. org/10.1016/j.saa.2014.07.085
- Atta D, Okasha A, Ibrahim M (2016) Setting up and calibration of simultaneous dual color wide field microscope for single molecule imaging. Der Pharma Chemica 8:76–82
- Li Z, Li Z, Ramos A, Boudreaux JP, Thiagarajan R, Mattison YB et al (2021) Detection of pancreatic cancer by indocyanine green-assisted fluorescence imaging in the first and second near-infrared windows. Cancer Commun 41:1431. https://doi.org/10.1002/cac2.12236
- Chung S, Fried D, Staninec M, Darling CL (2011) Multispectral near-IR reflectance and transillumination imaging of teeth. Biomed Opt Express 2:2804–2814. https://doi.org/10.1364/BOE.2.002804
- Atta D, Ismail MM, Battisha IK (2022) 3D laser Raman microspectroscopy of Er3+ and Yb3+ co-activated nano-composite phosphosilicate for industrial photonics applications. Opt Laser Technol 149:107761. https://doi.org/10.1016/j.optlastec.2021.107761
- Jeng M-J, Sharma M, Sharma L, Chao T-Y, Huang S-F, Chang L-B et al (2019) Raman spectroscopy analysis for optical diagnosis of oral cancer detection. J Clin Med 8:1313. https://doi.org/ 10.3390/jcm8091313

- Li Z, Li Z, Chen Q, Ramos A, Zhang J, Boudreaux JP et al (2021) Detection of pancreatic cancer by convolutional-neural-networkassisted spontaneous Raman spectroscopy with critical feature visualization. Neural Netw 144:455–464. https://doi.org/10. 1016/j.neunet.2021.09.006
- Li Z, Li Z, Chen Q, Zhang J, Dunham ME, McWhorter AJ et al (2022) Machine-learning-assisted spontaneous Raman spectroscopy classification and feature extraction for the diagnosis of human laryngeal cancer. Comput Biol Med 105617. https://doi. org/10.1016/j.compbiomed.2022.105617
- Shah KJ, Cohen-Gadol AA (2019) The application of FLOW 800 ICG videoangiography color maps for neurovascular surgery and intraoperative decision making. World Neurosurg 122:e186–ee97. https://doi.org/10.1016/j.wneu.2018.09.195
- Sandanaraj BS, Gremlich H-U, Kneuer R, Dawson J, Wacha S (2010) Fluorescent nanoprobes as a biomarker for increased vascular permeability: implications in diagnosis and treatment of cancer and inflammation. Bioconjugate Chem 21:93–101. https://doi. org/10.1021/bc900311h
- Saxena V, Sadoqi M, Shao J (2003) Degradation kinetics of indocyanine green in aqueous solution. J Pharm Sci 92:2090–2097. https://doi.org/10.1002/jps.10470
- Zhang D, Song X-j, Li S-y, Wang S-y, Chen B-j, Bai X-D et al (2016) Evaluation of liver function and electroacupuncture efficacy of animals with alcoholic liver injury by the novel imaging methods. Sci Rep 6:30119
- Sevick-Muraca EM, Lopez G, Reynolds JS, Troy TL, Hutchinson CL (1997) Fluorescence and absorption contrast mechanisms for biomedical optical imaging using frequency-domain techniques. Photochem Photobiol 66:55. https://doi.org/10.1111/j.1751-1097. 1997.tb03138.x
- Mokrousov MD, Novoselova MV, Nolan J, Harrington W, Rudakovskaya P, Bratashov DN et al (2019) Amplification of photoacoustic effect in bimodal polymer particles by self-quenching of indocyanine green. Biomed Opt Express 10:4775–4788. https:// doi.org/10.1364/BOE.10.004775
- Li X, Shen B, Yao X-Q, Yang D (2007) A small synthetic molecule forms chloride channels to mediate chloride transport across cell membranes. J Am Chem Soc 7264-7265. https://doi.org/10.1021/ja071961h
- Wang C, Chen S, Yu F, Lv J, Zhao R, Hu F et al (2021) Dualchannel theranostic system for quantitative self-indication and low-temperature synergistic therapy of cancer. Nanomicro Small 17:2007953. https://doi.org/10.1002/smll.202007953
- Harashima H, Iida S, Urakami Y, Tsuchihashi M, Kiwada H (1999) Optimization of antitumor effect of liposomally encapsulated doxorubicin based on simulations by pharmacokinetic/pharmacodynamic modeling. J Controlled Release: Official Journal of the Controlled Release Society 61:93–106. https://doi.org/10.1016/S0168-3659(99)00110-8
- Large DE, Abdelmessih RG, Fink EA, Auguste DTJADDR (2021) Liposome composition in drug delivery design, synthesis, characterization, and clinical application. Adv Drug Deliv Rev 176:113851. https://doi.org/10.1016/j.addr.2021.113851
- Jeong H-S, Lee C-M, Cheong S-J, Kim E-M, Hwang H, Na KS et al (2013) The effect of mannosylation of liposome-encapsulated indocyanine green on imaging of sentinel lymph node. J Liposome Res 23:291–297. https://doi.org/10.3109/08982104.2013.801488
- Suganami A, Iwadate Y, Shibata S, Yamashita M, Tanaka T, Shinozaki N et al (2015) Liposomally formulated phospholipid-conjugated indocyanine green for intra-operative brain tumor detection and resection. Int J Pharm 496:401–406. https://doi.org/10.1016/j.ijpharm.2015.10.001
- Li Z, Yao S, Xu J, Wu Y, Li C, He Z (2018) Endoscopic nearinfrared dental imaging with indocyanine green: a pilot study. Ann N Y Acad Sci 1421:88–96. https://doi.org/10.1111/nyas.13674



140 Page 8 of 8 Lasers in Medical Science (2023) 38:140

Li Z, Hartzler T, Ramos A, Osborn ML, Li Y, Yao S et al (2020) Optimal imaging windows of indocyanine green-assisted near-infrared dental imaging with rat model and its comparison to X-ray imaging. J Biophotonics e201960232. https://doi.org/10.1002/jbio.201960232

- Chatterjee DK, Rufaihah AJ, Zhang Y (2008) Upconversion fluorescence imaging of cells and small animals using lanthanide doped nanocrystals. Biomaterials 29:937–943. https://doi.org/10.1016/j.biomaterials.2007.10.051
- Lu F, Zhao T, Sun X, Wang Z, Fan Q, Huang W (2021) Rare-earth doped nanoparticles with narrow NIR-II emission for optical imaging with reduced autofluorescence. Chem Res Chin Univ 37:943

  –950
- Jarmo TA, Ilkka K, Aki L, Tommi P, Thomas S, Valery VT et al (2012) A review of indocyanine green fluorescent imaging in surgery. International Journal of Biomedical Imaging. J Biomed Imaging 2012;7. https://doi.org/10.1155/2012/940585
- Newton AD, Predina JD, Corbett CJ, Frenzel-Sulyok LG, Xia L, Petersson EJ et al (2019) Optimization of second window indocyanine green for intraoperative near-infrared imaging of thoracic malignancy. J Am Coll Surg 228:188–197. https://doi.org/10. 1016/j.jamcollsurg.2018.11.003
- Li Z, Holamoge YV, Li Z, Zaid W, Osborn ML, Ramos A et al (2020) Detection and analysis of enamel cracks by ICG-NIR fluorescence dental imaging. Ann N Y Acad Sci 1475:52–63. https:// doi.org/10.1111/nyas.14374
- Li Z, Li Z, Holamoge YV, Zaid W, Osborn ML, Bhatta S et al (2021) Mouthwash to deliver indocyanine green for near infrared dental fluorescence imaging. IEEE J Sel Top Quantum Electron 27:1–8. https://doi.org/10.1109/JSTQE.2020.2995659

- Li Z, Zaid W, Hartzler T, Ramos A, Osborn ML, Li Y et al (2019) Indocyanine green-assisted dental imaging in the first and second near-infrared windows as compared with X-ray imaging. Ann N Y Acad Sci 1448:42–51. https://doi.org/10.1111/nyas.14086
- Li Z, Yao S, Xu J (2019) Indocyanine-green-assisted near-infrared dental imaging-the feasibility of in vivo imaging and the optimization of imaging conditions. Sci Rep 9:1–8
- Zhou X, Li H, Shi C, Xu F, Zhang Z, Yao Q et al (2020) An APNactivated NIR photosensitizer for cancer photodynamic therapy and fluorescence imaging. Biomaterials 253. https://doi.org/10. 1016/j.biomaterials.2020.120089
- Ge L, Möhwald H, Li J (2003) Phospholipid liposomes stabilized by the coverage of polyelectrolyte. Colloids Surf A Physicochem Eng Asp 221:49–53. https://doi.org/10.1016/S0927-7757(03) 00106-7
- Li Z, Li Z, Zaid W, Osborn ML, Li Y, Yao S et al (2022) Mouthwash as a non-invasive method of indocyanine green delivery for near-infrared fluorescence dental imaging. J Biomed Opt 27:066001. https://doi.org/10.1117/1.JBO.27.6.066001

**Publisher's note** Springer Nature remains neutral with regard to jurisdictional claims in published maps and institutional affiliations.

Springer Nature or its licensor (e.g. a society or other partner) holds exclusive rights to this article under a publishing agreement with the author(s) or other rightsholder(s); author self-archiving of the accepted manuscript version of this article is solely governed by the terms of such publishing agreement and applicable law.

